Dynamics of multiple interacting excitatory and inhibitory populations with delays

Christopher M. Kim [1,*] Ulrich Egert,[1,2] and Arvind Kumar [1,3,†]

[1]*Bernstein Center Freiburg, 79104 Freiburg, Germany*

[2]*Biomicrotechnology, IMTEK—Department of Microsystems Engineering, University of Freiburg, 79110 Freiburg, Germany*

[3]*Department of Computational Science and Technology, School for Electrical Engineering and Computer Science, KTH Royal Institute of Technology, Lindstedtsvägen 3, 11428 Stockholm, Sweden*

(Received 27 June 2018; revised 13 May 2020; accepted 15 July 2020; published 12 August 2020)

A network consisting of excitatory and inhibitory (EI) neurons is a canonical model for understanding local cortical network activity. In this study, we extended the local circuit model and investigated how its dynamical landscape can be enriched when it interacts with another excitatory (E) population with long transmission delays. Through analysis of a rate model and numerical simulations of a corresponding network of spiking neurons, we studied the transition from stationary to oscillatory states by analyzing the Hopf bifurcation structure in terms of two network parameters: (1) transmission delay between the EI subnetwork and the E population and (2) inhibitory couplings that induced oscillatory activity in the EI subnetwork. We found that the critical coupling strength can strongly modulate as a function of transmission delay, and consequently the stationary state can be interwoven intricately with the oscillatory state. Such a dynamical landscape gave rise to an isolated stationary state surrounded by multiple oscillatory states that generated different frequency modes, and cross-frequency coupling developed naturally at the bifurcation points. We identified the network motifs with short- and long-range inhibitory connections that underlie the emergence of oscillatory states with multiple frequencies. Thus, we provided a mechanistic explanation of how the transmission delay to and from the additional E population altered the dynamical landscape. In summary, our results demonstrated the potential role of long-range connections in shaping the network activity of local cortical circuits.

DOI: 10.1103/PhysRevE.102.022308

I. INTRODUCTION

The brain is organized as a network of highly specialized subnetworks. Each of the subnetworks consists of a large number of excitatory (E) and inhibitory (I) neurons communicating via spikes. Randomly connected networks of excitatory and inhibitory neurons have been a popular and useful model to study the dynamical states and information processing in local networks of the brain. Previous work has demonstrated that balance of excitation and inhibition (EI balance) is a crucial variable that determines two qualitatively different states of network activity. When excitation and inhibition are balanced, cancellation of excitatory and inhibitory synaptic inputs to a neuron leads to asynchronous and nearly Poisson-type spiking [1]. A mismatch between excitation and inhibition (in amplitude or timing) could result in various activities such as perfect synchrony or pattern formations. In this study, we will consider an oscillatory state in which the population firing rate oscillates while individual neurons spike irregularly [2–4]. Both asynchronous and oscillatory network states are considered to play important roles in cortical processing; the asynchronous activity of the balanced state provides a suitable substrate to perform complex computations [5,6], balanced amplification [7,8], and propagation of rate- and time-coded signals [9], and oscillatory rhythms play a crucial role in selective routing information across multiple brain areas [10–13].

Besides the EI balance, spike propagation time delays introduce various complex effects on the network activity dynamics. For instance, delays may destabilize the balanced state of spiking networks [2–4], enrich the bifurcation structure of spatially extended neural field models by introducing novel dynamical states [14,15], and gate the propagation of spiking activity [16]. Moreover, by suitably tuning the delays, oscillations can be enhanced and suppressed [17–19].

Experimental studies have shown that neurons in several brain regions communicate with each other via long synaptic delays [20–22]. Although long-range excitatory connections have been known for some time, recent experimental studies have also found long-range inhibitory connections. In particular, the long-range inhibition has been found to exist between the entorhinal cortex and hippocampus with transmission delay of 4.5 ms [23]. These long-range GABAergic axons can enhance rhythmic θ activity in target areas [23]. In another recent study, GABAergic CA1 neurons in the hippocampus have been shown to form long-range inhibitory connections to pyramidal neurons in the cortical area [24]. In addition, projections from subcortical regions (which are largely made of inhibitory neurons, e.g., globus pallidus, amygdala) to the cortex are also long range and involve long delays [25–27].

In this study, we investigated the potential role of such long transmission delays in shaping the dynamical landscape

*Corresponding author: chrismkkim@gmail.com; Present address: Laboratory of Biological Modeling, NIDDK/NIH, Bethesda, MD, USA.

†Corresponding author: arvkumar@kth.se

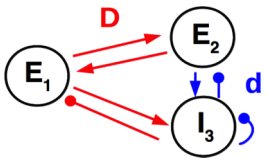

FIG. 1. The connectivity structure of the $E_1E_2I_3$ network.

of local cortical activity. To this end, we considered a three-population network (Fig. 1). This is a simple extension of the recurrently connected network of excitatory (E) and inhibitory (I) neurons—a generic and standard model of networks found in the neocortex [1–4,9] as an additional excitatory population is introduced in the network. The simplicity of the three-population network enabled us to rigorously examine and understand the network dynamics that arise from long delays. This model also naturally introduced long-range inhibition, whose existence is supported by recent experimental findings [23,24,28].

Through analysis and simulations of our network models, we show that the asynchronous state can be interwoven intricately with multiple oscillatory states when the EI network was strongly coupled to a third excitatory population with delays. Such dynamical landscapes naturally gave rise to cross-frequency oscillations in parameter regime where multiple oscillatory states merged. Thus, we revealed effects of long inhibitory delays on local network dynamics. Our study demonstrates the rich dynamic repertoire of interacting subnetworks in the presence of long delays and paves the way to study a network of multiple subnetworks.

II. NETWORK MODEL

The network consisted of two excitatory populations (E_1, E_2) and one inhibitory population (I_3). The E_2I_3 subnetwork was the standard EI network [2], which was reciprocally connected to the E_1 population (Fig. 1). We did not include recurrent excitatory connections within E_1 and E_2 because we focused on oscillatory network activity generated by the excitatory-inhibitory and inhibitory-inhibitory couplings. We referred to the connectivity parameters between E_1 and E_2I_3 as "lateral" and those within the E_2I_3 subnetwork as "local." The population E_1 was considered to be located at a farther distance; therefore, the transmission delay D between E_1 and E_2I_3 was larger than the transmission delay d within the E_2I_3 subnetwork. In this work, we investigated the effect of long transmission delays and inhibitory connections from I_3 to E_1, E_2 and itself on network oscillations.

To study the network dynamics analytically, we considered a rate model that described the firing rate dynamics of three populations and compared the results with numerical simulations of a comparable network with spiking neurons.

A. Firing rate model

The rate model was described as a set of delay differential equations,

$$\tau_1\dot{r}_1(t) = -r_1(t) + [J_{11}s_{11}(t) + J_{12}s_{12}(t) - J_{13}s_{13}(t) + I_1]_+,$$
$$\tau_2\dot{r}_2(t) = -r_2(t) + [J_{21}s_{21}(t) + J_{22}s_{22}(t) - J_{23}s_{23}(t) + I_2]_+,$$
$$\tau_3\dot{r}_3(t) = -r_3(t) + [J_{31}s_{31}(t) + J_{32}s_{32}(t) - J_{33}s_{33}(t) + I_3]_+, \quad (1)$$

where J_{ab} is the coupling strength of the connection from population b to population a, I_a is an external input, and the activation function $[x]_+ = x$ if $x > 0$ and $= 0$ otherwise. We let $J_{11} = J_{22} = 0$ because there were no recurrent excitatory connections. The dynamics of synaptic current from b to a obeyed

$$\tau_d\dot{s}_{ab} = -s_{ab} + r_b(t - D_{ab}) \quad a, b \in \{1, 2, 3\}, \quad (2)$$

where τ_d is a decay time constant and D_{ab} is a transmission delay from b to a.

The connections between E_1 and E_2I_3 had a transmission delay, D, and the connections within the E_2I_3 subnetwork had a transmission delay, d; $D = D_{12} = D_{21} = D_{13} = D_{31}$ and $d = D_{23} = D_{32} = D_{33}$.

B. Network model with spiking neurons

For the spiking network model, we considered a network of randomly connected leaky integrate-and-fire (LIF) neurons where E_1, E_2, and I_3 populations consisted of $N_1 = N/2$, $N_2 = N$, and $N_3 = N/4$ neurons ($N = 10\,000$), respectively. The membrane potential of neuron i in population a obeyed

$$\tau_{ma}\dot{V}_i(t) = -V_i(t) + \mu_a + \sigma_a\xi_i(t) + \frac{J_{a1}}{pN_1}\sum_{j\in E_1} s_{ij} + \frac{J_{a2}}{pN_2}\sum_{j\in E_2} s_{ij} - \frac{J_{a3}}{pN_3}\sum_{j\in I_3} s_{ij} \quad (3)$$

and elicited an action potential when V_i reached a threshold V_{th} (20 mV), and then reset to V_r (10 mV). Here, p (0.1) is connection probability, τ_{ma} (20 ms for $a = 1, 2$; 10 ms for $a = 3$) is a membrane time constant, J_{ab} is total postsynaptic potential of synaptic connections from population b to population a, μ_a is an external input, and $\sigma_a\xi_i$ is Gaussian white noise with mean zero and variance σ_a^2.

Every neuron received the same number pN_a of recurrent synaptic inputs from randomly selected neurons in populations $a = 1, 2, 3$. However, the neurons in E_1 and E_2 did not receive synaptic inputs from other neurons in the same population (i.e., E_1-E_1 and E_2-E_2 did not exist). The strength of individual synapses from neuron j in population b to neuron i in population a was given by $J_{ab}/(pN_b)$.

The synaptic current s_{ij} decayed exponentially upon receiving a spike from a presynaptic neuron j in population b:

$$\tau_d\dot{s}_{ij} = -s_{ij} + \tau_{ma}\sum_{t_i^k<t}\delta\left(t - t_i^k - D_{ab}\right),$$

where τ_d (1 ms) is synaptic decay rate, t_i^k is the spike time of presynaptic neurons, and D_{ab} is the transmission delay from neurons in population b to neurons in population a. As in the firing rate model, the connections between E_1 and E_2I_3 had a transmission delay, D, and the connections within the E_2I_3 subnetwork had a transmission delay, d.

Following the previous studies [2,4,5], we estimated the steady-state firing rate using the Fokker-Planck approach,

which meant solving a system of three nonlinear equations in a self-consistent manner.

$$r_a = \Psi_a(X_a, Y_a), \quad a = 1, 2, 3, \tag{4}$$

where

$$\Psi_a(X_a, Y_a) = \left[\tau_{ma}\sqrt{\pi}\int_{(V_r - X_a)/Y_a}^{(V_{\rm th} - X_a)/Y_a} e^{t^2}(1 + \mathrm{erf}(t))dt\right]^{-1},$$
$$X_a = \mu_a + J_{a1}r_1 + J_{a2}r_2 - J_{a3}r_3,$$
$$Y_a = \sqrt{\sigma_a^2 + J_{a1}^2 r_1 + J_{a2}^2 r_2 + J_{a3}^2 r_3}.$$

Here, r_a is the population-averaged firing rate, X_a is the mean synaptic input, and Y_a^2 is the variance of total synaptic input to a neuron.

In the following network simulations, we adjusted the mean (μ_a) and variance (σ_a^2) of external inputs to obtain the same steady-state firing rate ($r_e = 5$ Hz, $r_i = 10$ Hz) for different network configurations. To generate consistent firing rates and synaptic noise across networks with different coupling strengths, we fixed the standard deviation of the total synaptic current ($Y_a = 5$ mV; $a \in 1, 2, 3$) injected into each population for all networks and derived the mean external inputs μ_a that generated the desired firing rates by solving Eq. (4) numerically using the threshold integration method [29]. When given the coupling strength J's and the desired firing rates r's, Y_a did not match with the assumed value 5 mV, we varied the variance of external inputs σ_a^2 such that Y_a was equal to the assumed value of 5 mV. External inputs (I_a) to the rate model were adjusted similarly to maintain same r_a across networks with different coupling strengths. Firing rate equations [Eq. (1)] were solved using MATLAB's delay differential equation solver, dde23. The simulation of networks with spiking neurons was performed using the NEST simulation tool [30].

III. OSCILLATORY DYNAMICS IN THE THREE POPULATION MODEL

A. Linear stability of the steady state

To characterize how the lateral delay D affected the emergence of oscillatory activity within the E_2I_3 subnetwork, we performed linear stability analysis of the steady state of the rate model and the spiking network model. We added a small perturbation term to the steady-state firing rate such that $r_a(t) = r_{a0} + \delta r_a e^{\lambda t}$. The rate perturbation induced a perturbation in the synaptic current:

$$\delta s_{ab}(t) = \Sigma_{ab}(\lambda)\delta r_b e^{\lambda t}, \tag{5}$$

where the synaptic kernel [Eq. (2)] in frequency domain is given by

$$\Sigma_{ab}(\lambda) = \frac{e^{-\lambda D_{ab}}}{1 + \lambda\tau_d}. \tag{6}$$

From Eq. (5), we obtained the perturbation of total input to population a

$$\delta I_a(t) = J_{a1}\delta s_{a1}(t) + J_{a2}\delta s_{a2}(t) - J_{a3}\delta s_{a3}(t). \tag{7}$$

Finally, the new output rate of the network in response to the input rate perturbation was given by

$$\delta r_a e^{\lambda t} = R_a(\lambda)\delta I_a(t). \tag{8}$$

Similar to the synapse, the neuron population also acted like a frequency filter which can be written as, for the rate model,

$$R_a^{\rm RM}(\lambda) = \frac{1}{1 + \tau_a\lambda} \tag{9}$$

and, for LIF neurons, $R_a^{\rm LIF}$ can be either calculated numerically using the threshold integration method [29] or by hypergeometric functions [2,4].

Combining Eqs. (5), (7), and (8), we obtained a system of three linear equations in δr_a, $a = 1, 2, 3$, which had nontrivial solutions when the determinant of following matrix was zero:

$$0 = \begin{vmatrix} -1 & A_{12}(\lambda) & -A_{13}(\lambda) \\ A_{21}(\lambda) & -1 & -A_{23}(\lambda) \\ A_{31}(\lambda) & A_{32}(\lambda) & -[1 + A_{33}(\lambda)] \end{vmatrix}, \tag{10}$$

where $A_{ab}(\lambda) = R_a(\lambda)J_{ab}\Sigma_{ab}(\lambda)$. Rearranging Eq. (10), we obtained

$$0 = (1 - A_{12}A_{21})(1 + \underbrace{A_{33}}_{J_{33}\text{ coupling}})$$
$$+ \underbrace{A_{32}A_{23} + A_{31}A_{12}A_{23}}_{J_{23}\text{ coupling}} \quad \text{(Fast inhibition)}$$
$$+ \underbrace{A_{31}A_{13} + A_{32}A_{21}A_{13}}_{J_{13}\text{ coupling}} \quad \text{(Slow inhibition)}. \tag{11}$$

Equation (11) describes network motifs in the $E_1E_2I_3$ model that can induce network oscillations. The two first lines of Eq. (11) consist of motifs that receive fast inhibition with short delay d via two different pathways. The local inhibitory coupling J_{33} is responsible for generating oscillatory activity via the monosynaptic A_{33} loop, whereas the inhibitory coupling J_{23} is responsible for generating oscillatory activity via disynaptic $A_{32}A_{23}$ and trisynaptic $A_{31}A_{12}A_{23}$ loops. The third line of Eq. (11) consists of network motifs that receive slow inhibition. In this case, the inhibitory coupling J_{13} is responsible for generating oscillatory activity via disynaptic $A_{31}A_{13}$ and trisynaptic $A_{32}A_{21}A_{13}$ loops with long delay D.

B. Transition to oscillatory states

To obtain analytical estimates of a Hopf bifurcation, which marks the transition from a steady state to an oscillatory state, we substituted $\lambda = i\omega$ into Eq. (11) to find bifurcation points as a function of D and J_{33} (or D and J_{23}). A similar calculation was performed in Ref. [4]. We denoted the amplitude and the phase of the population response function $R_a(i\omega)$ as H_a and ϕ_a, respectively, i.e., $R_a(i\omega) = H_a(\omega)\exp[-i\phi_a(\omega)]$. The amplitude and phase of the synaptic kernel $\Sigma_{ab}(i\omega)$ were denoted as H_s and ϕ_s, respectively, i.e., $\Sigma_{ab} = H_s(\omega)\exp[-i\phi_s(\omega) - iD_{ab}\omega]$, where $D_{ab}\omega$ is the phase shift due to a transmission delay. To simplify notations, we let $\Phi_a = \phi_a + \phi_s$ be the sum of phase shifts due to population response of a and synaptic dynamics (without a delay), and $\Phi_{ab} = \Phi_a + \Phi_b$, etc.

The real part of Eq. (11) is

$$\begin{aligned}0 = {} & 1 - c_r \cos(\Phi_{12} + 2D\omega) + c_i[\cos(\Phi_3 + d\omega) \\ & - c_r \cos(\Phi_{123} + 2D\omega + d\omega)] + c_{p_d} \cos(\Phi_{23} + 2d\omega) \\ & + c_{p_t} \cos(\Phi_{123} + 2D\omega + d\omega) \\ & + c_t \cos(\Phi_{123} + 2D\omega + d\omega) + c_d \cos(\Phi_{13} + 2D\omega)\end{aligned} \tag{12}$$

and its imaginary part is

$$\begin{aligned}0 = {} & - c_r \sin(\Phi_{12} + 2D\omega) \\ & + c_i[\sin(\Phi_3 + d\omega) - c_r \sin(\Phi_{123} + 2D\omega + d\omega)] \\ & + c_{p_d} \sin(\Phi_{23} + 2d\omega) + c_{p_t} \sin(\Phi_{123} + 2D\omega + d\omega) \\ & + c_t \sin(\Phi_{123} + 2D\omega + d\omega) + c_d \sin(\Phi_{13} + 2D\omega),\end{aligned} \tag{13}$$

where $c_r = J_{12}J_{21}H_1H_2H_s^2$ is the bidirectional coupling between E_1 and E_2, $c_i = J_{33}H_3H_s$ is the I_3-I_3 coupling, $c_{p_d} = J_{32}J_{23}H_2H_3H_s^2$ and $c_{p_t} = J_{31}J_{12}J_{23}H_1H_2H_3H_s^3$ are the disynaptic and trisynaptic E_2-I_3 couplings, respectively, and $c_d = J_{13}J_{31}H_1H_3H_s^2$ and $c_t = J_{32}J_{21}J_{13}H_1H_2H_3H_s^3$ are the disynaptic and trisynaptic E_1-I_3 couplings, respectively.

In the following calculations, J_{33} and D were the two bifurcation parameters, and we sought to express them as functions of ω (see Appendix A for the derivation of other critical couplings). First, to write J_{33} as a function of ω, we removed D from Eqs. (12) and (13) by moving three (two) terms in Eq. (12) [Eq. (13)] that did not include D to the other side of the equation, squaring both sides of each equation, and then adding two equations to obtain a quadratic equation of c_i,

$$0 = Ac_i^2 + 2Bc_i + C.$$

Then,

$$c_i^{\pm} = \frac{1}{A}(-B \pm \sqrt{B^2 - AC})$$

or

$$J_{I_3I_3}^{\pm} = c_i^{\pm} / (H_3H_s), \tag{14}$$

where

$$\begin{aligned}A &= c_r^2 - 1, \\ B &= -c_r(c_{p_t} + c_t) + (c_r^2 - 1)\cos(\Phi_3 + d\omega) \\ &\quad - (c_rc_d + c_{p_d})\cos(\Phi_2 + d\omega), \\ C &= 2\{(c_{p_t} + c_t)[-c_r \cos(\Phi_3 + d\omega) + c_d \cos(\Phi_2 + d\omega)] \\ &\quad - c_{p_d} \cos(\Phi_{23} + 2d\omega) - c_rc_d \cos(\Phi_3 - \Phi_2)\} \\ &\quad + c_r^2 - c_{p_d}^2 + c_{p_t}^2 + c_d^2 + c_t^2 + 2c_{p_t}c_t - 1.\end{aligned}$$

Next, to write D as a function of ω, we invoked trigonometric identities in Eqs. (12) and (13) to derive a system of equations to explicitly solve for $\cos 2D\omega$ and $\sin 2D\omega$:

$$\begin{bmatrix} M_{11} & M_{12} \\ M_{21} & M_{22} \end{bmatrix} \begin{bmatrix} \cos 2D\omega \\ \sin 2D\omega \end{bmatrix} = \begin{bmatrix} P \\ Q \end{bmatrix},$$

where

$$\begin{aligned}M_{11} &= -M_{22} = -c_r \cos\Phi_{12} - c_rc_i \cos(\Phi_{123} + d\omega) \\ &\quad + c_{p_t} \cos(\Phi_{123} + d\omega) + c_d \cos\Phi_{13} \\ &\quad + c_t \cos(\Phi_{123} + d\omega), \\ M_{12} &= M_{21} = c_r \sin\Phi_{12} + c_rc_i \sin(\Phi_{123} + d\omega) \\ &\quad - c_{p_t} \sin(\Phi_{123} + d\omega) - c_d \sin\Phi_{13} \\ &\quad - c_t \sin(\Phi_{123} + d\omega), \\ P &= -1 - c_i \cos(\Phi_3 + d\omega) - c_{p_d} \cos(\Phi_{23} + 2d\omega) \\ Q &= c_i \sin(\Phi_3 + d\omega) + c_{p_d} \sin(\Phi_{23} + 2d\omega).\end{aligned}$$

Substituting $c_i^{\pm}$ calculated above, we obtained an expression for the lateral delay at the Hopf bifurcation

$$D^{\pm} = \frac{1}{2\omega} \text{atan}\left(\frac{-M_{21}^{\pm}P^{\pm} + M_{11}^{\pm}Q^{\pm}}{M_{22}^{\pm}P^{\pm} - M_{12}^{\pm}Q^{\pm}}\right). \tag{15}$$

In the following sections, we describe the Hopf bifurcation lines ($D^{\pm}, J_{33}^{\pm}$) that satisfy both Eqs. (13) and (12) by varying ω and compare the analytical results with numerical solutions of delay differential equations for the rate model and simulations of networks of leaky integrate-and-fire neurons for the spiking network model.

IV. DYNAMICAL STATES OF $E_1E_2I_3$ NETWORK

In the following, we refer to the (nonoscillatory) steady state as S and three oscillatory states as O_1, O_2, and O_3. As described in Eq. (11), three types of inhibitory couplings J_{13}, J_{23}, and J_{33} are responsible for generating the oscillatory states O_1, O_2, and O_3, respectively.

A. Network activity states

To characterize different dynamical states of the three-population network, we systematically varied the I_3-I_3 coupling (J_{33}) and the delay in lateral connections (D) (Fig. 2). For each parameter pair (J_{33}, D), we simulated the network for 1.2 s and measured the standard deviation of the population rates to estimate whether the network exhibited oscillations. The external input to each population was adjusted to maintain constant population rates across different network setups (5 Hz for excitatory and 10 Hz for inhibitory spiking neurons) while other network parameters remained fixed. For both network models, the standard deviation of each population rate was normalized by its means and averaged over three populations to obtain the coefficient of variation of the population activity. When the network was oscillating, the standard deviation of the network activity was higher as the network activity waxed and waned. This is, however, only an indirect measure and may not directly imply oscillations; therefore, we also examined the spectrum of the population activity (Fig. 4).

For a fixed value of D, the network exhibited three distinct states, O_1, S, and O_3, as we varied J_{33}. (Hopf bifurcation estimates are shown as white lines in Fig. 2.) The estimates of the network activity states closely matched with the states obtained from a corresponding simulations of a network of spiking neurons [Figs. 2(a) and 2(b)]. For low values of J_{33}, O_1 was observed, which is characterized by slow

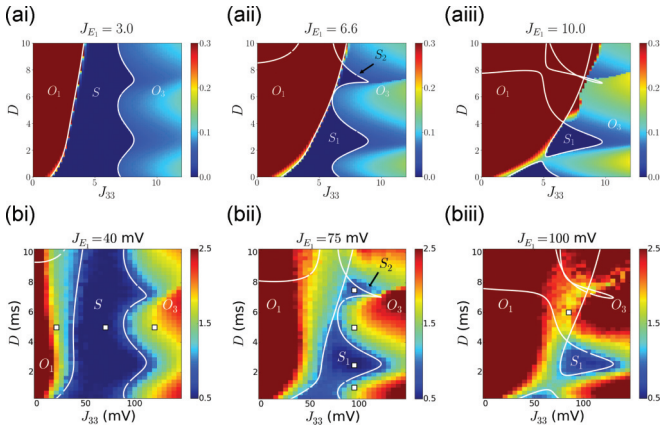

FIG. 2. Bifurcation diagrams of **(a)** rate model and **(b)** spiking network model as a function of I_3-I_3 coupling J_{33} and lateral delay D. The strength of synaptic projection, $J_{E_1}(= J_{21}, J_{31})$, from E_1 to E_2I_3 is weak (a.i, b.i), intermediate (a.ii, b.ii) and strong (a.iii, b.iii). For the rate model, $J_{12} = 0.5, J_{13}, J_{23}, J_{32} = 2,\ d = 2.5,\ \tau_d = 0$. For the spiking network model, the total (individual) synaptic weights $J_{12} = 30(0.03), J_{13} = 80(0.32), J_{23}, J_{32} = 50(0.2, 0.05)$ mV. Note that the weights of individual synapses from neuron j in population b to neuron i in population a is given by $J_{ab}/(pN_b)$ (Eq. 3), so that I_3 to I_3 synaptic weights are between 0 and 0.6 mV. Local delay $d = 2.5$ ms, and synaptic decay time $\tau_d = 1$ ms. Color bars show the coefficient of variations of the network models (See text for details). White lines show analytical estimates of a Hopf bifurcation (Eqs. 14 and 15).

frequency oscillations (≈25 Hz) mediated by the E_1-I_3 loop with lateral delay $D = 5$ ms [see white squares in Fig. 2(b)(i) and the corresponding spiking activity in Fig. 4(a), top]. For moderate values of J_{33}, oscillations vanished and a nonoscillatory state emerged (S) in which neurons fired asynchronously and the population firing rate randomly fluctuated around the steady state (akin to the asynchronous irregular state of Ref. [2]). Finally, for very strong inhibitory coupling (high J_{33}), the nonoscillatory state was transformed into another oscillatory state O_3, which was characterized by high-frequency oscillations (≈100 Hz) mediated by the local I_3-I_3 loop with local delay $d = 2.5$ ms. The E_1-I_3 interaction that gave rise to the O_1 state shared the same dynamic mechanism as the

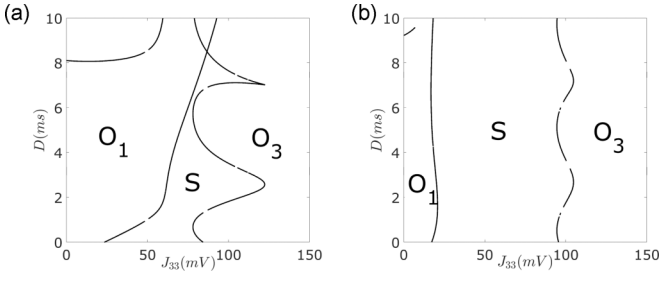

FIG. 3. Effects of lateral inhibition on the dynamic landscape. (a) Strong modulation at the interface of S and O_3 in a network configuration identical to Fig. 2(b)(ii). (b) The modulation of bifurcation line from S to O_3 is significantly reduced as a result of decreasing the coupling strength of lateral inhibition (i.e., J_{13}) by a factor of 0.3. All other network parameters were identical to panel (a).

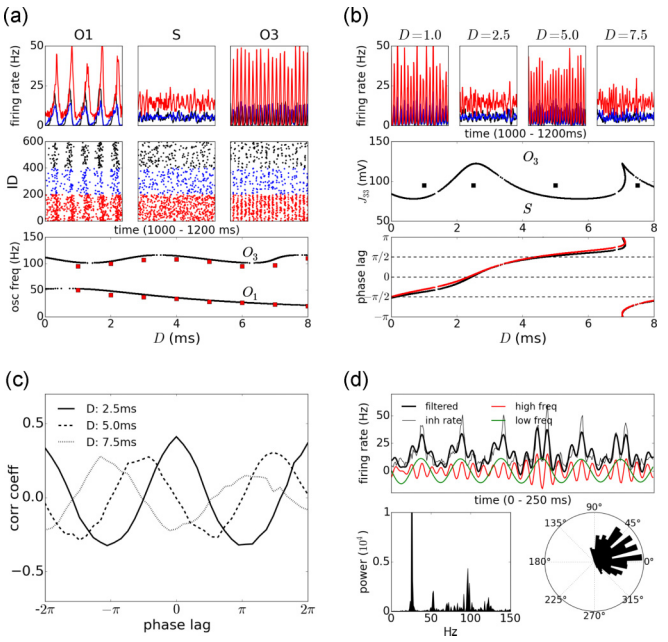

FIG. 4. (a) (Top) Instantaneous firing rate of E_1 (black), E_2 (blue), and I_3 (red) populations in S, O_1, and O_3 states; (middle) spike raster of the corresponding spiking activity. (Bottom) Oscillation frequency of O_1 and O_3 states as a function of lateral delay; black, analysis; red, simulations. (b) (Top) Alternation between S and O_3 states due to the lateral delay, corresponding to white squares in Fig. 2(b)(ii)). (Middle) Analytical estimates of critical $J_{I_3I_3}$ (black line) and network states corresponding to the top row (black squares). (Bottom) Analytical estimate of the phase lag $\Delta\phi_{31}$ of I_3 with respect to E_1 in the O_3 state; black, full network [Eq. (B1)], red, simplified E_1I_3 network [Eq. 19]. (c) Cross correlation of mean firing rate of E_1 and I_3, calculated using simulation results from part (b). (d) Cross-frequency coupling appears when O_1 and O_3 merge; (top) mean firing rate of I_3 (gray), its high-frequency (red) and low-frequency (green) components, and the sum of high and low frequencies (black); (left bottom) power spectrum of I_3 mean firing rate; (right bottom) correlation between fast oscillation amplitude (black bar) and slow oscillation phase (angle).

pyramidal-interneuron (PING) oscillations [31,32], and the I_3-I_3 interaction of the O_3 state was similar to the interneuron (ING) oscillations [33,34].

As the lateral delay D was increased, the region of O_1 monotonically increased and the state S was observed at higher values of J_{33}. The lateral delay D had a more dramatic effect on the emergence of the state O_3. The value of J_{33} at which the oscillatory state O_3 was observed varied in a periodic manner as D was increased [see the interface of O_1 and S and that of O_3 and S in Figs. 2(a)(i) and 2(b)(i)]. While the oscillation frequency in O_1 state decreased monotonically with D, the oscillation frequency in O_3 state was independent of D [Fig. 4(a), bottom; black lines indicate analysis and red squares indicate simulations].

Next, we examined whether the long-range inhibition from I_3 to E_1 (i.e., J_{13}) was responsible for the periodic modulation of the boundary that separated oscillatory (O_3) and nonoscillatory (S) states (J_{33}^{crit}). To this end, we reduced the coupling strength of long-range inhibition, i.e., J_{13}, of the network

shown in Fig. 2(b)(ii) by a factor of 0.3 while keeping other network parameters fixed. We found that the strong modulation of the critical J_{33}^{crit} was significantly reduced [compare the interface of S and O_3 in Figs. 3(a) and 3(b)]. A similar effect was observed when connections from E_1 to E_2I_3 were reduced by a factor of 0.53 [compare Figs. 2(b)(i) and 2(b)(ii)]. These observations suggested that the strong coupling between E_1 and E_2I_3, mediated by the long-range inhibition, gave rise to the periodic modulation of the bifurcation line between S and O_3.

To better understand this phenomenon, we next examined the oscillation dynamics at the interface of the nonoscillatory state S and the oscillatory state O_3.

B. Modulation of critical I_3-I_3 coupling due to lateral delay

To gain intuition on why the local coupling J_{33} may depend on lateral delays D, we reduced the subnetwork E_2I_3 to an inhibitory population I_3. This effectively assumed that the subnetwork E_2I_3 operated in an inhibition dominated regime. By solving Eqs. (12) and (13) for the critical I_3-I_3 coupling in terms of D, we obtained

$$J_{33} = \frac{[1 - 2c_d(\omega)\cos(\Phi_{13} + 2D\omega + \pi) + c_d(\omega)^2]^{1/2}}{H_3(\omega)H_s(\omega)}. \tag{16}$$

From Eq. (16), the reduced network model suggested that the critical J_{33} modulated periodically as a function of D, and the period of modulation $T = \pi/\omega^* = 1/(2f^*)$ was determined by the frequency of network oscillations, $\omega^* = 2\pi f^*$. [Here we assumed that the oscillation frequency at the transition to O_3 state depends weakly on D; in other words, $\omega(D) \equiv \omega^*$ on the boundary of O_3 as shown in Fig. 4(a) (bottom).] Moreover, the maximum of J_{33} was attained at

$$(2n + 1)\pi = \Phi_{13}(\omega^*) + 2D\omega^* + \pi, \tag{17}$$

and the minimum of J_{33} at

$$2n\pi = \Phi_{13}(\omega^*) + 2D\omega^* + \pi \tag{18}$$

for $n = 0, \pm1, ...$, where $\Phi_{13}(\omega^*) + 2D\omega^*$ is the total phase shift induced by the bidirectional lateral connections between E_1 and I_3, and π appears due to the inhibitory coupling. In other words, Eq. (17) [Eq. (18)] suggested that the critical J_{33} reached its maximum (minimum) when the network oscillation relayed through the lateral connections was antiphase (in phase) to the oscillations generated in I_3.

Conceptually, this phenomenon can be understood as follows. If oscillatory activity relayed through lateral connections is in phase with oscillatory activity generated by the local I_3-I_3 loop, weak coupling is sufficient to induce network-wide oscillations. On the other hand, if the relayed network activity is antiphasic to locally generated activity, stronger coupling is required to overcome the suppression of the local activity by the relayed activity. Because changing the lateral delay shifts the phase of relayed activity continuously, the critical coupling strength modulates quasiperiodically with a period determined by the oscillation frequency. In Fig. 2(b)(i), for instance, the period of O_3 boundary ($T \approx 5$ ms) is determined by the oscillation frequency of O_3 state [$f \approx 100$ Hz, Fig. 4(a), bottom]: $T \approx 1/(2f)$ as predicted by Eq. (16).

We also calculated the relative phase $\Delta\phi_{31}^{\max}$ ($\Delta\phi_{31}^{\min}$) of I_3 population rate with respect to the E_1 population rate at the maximum (minimum) of J_{33}. For the reduced network model, the phase lag was given by

$$\Delta\phi_{31} = -\pi + \Phi_1 + D\omega, \tag{19}$$

and at the max and min of J_{33},

$$\begin{aligned} \Delta\phi_{31}^{\max} &= (n-1)\pi, \\ \Delta\phi_{31}^{\min} &= \left(n - \tfrac{1}{2}\right)\pi, \quad n = 0, \pm1, \pm2, ..., \end{aligned} \tag{20}$$

where we used Eqs. (17) and (18) to evaluate $D\omega^*$ and assumed that the phase shifts due to population response functions are equal, i.e., $\Phi_1 = \Phi_3$. We then verified numerically that the phase lag in the full $E_1E_2I_3$ network can be approximated by that of the reduced network [Fig. 4(b), bottom; black, full network; red, reduced network]. See Appendix B for the derivation of phase lags in the full and reduced network models.

C. Cross-frequency coupling in the oscillatory activity

When the coupling strength between the lateral excitatory population (E_1) and the local excitatory-inhibitory network (E_2I_3) was further increased, oscillatory dynamics at different frequencies started merging and generated oscillations with multiple frequency with codependence between different oscillation frequencies.

At the intermediate step toward the emergence of multifrequency oscillations, we examined how the strength of connections from the excitatory population E_1 (J_{E_1}) affected the landscape of the network states. First, we found that increase in J_{E_1} increased the region of the state O_1. Second, J_{E_1} also increased the modulation in the boundary of state O_3. Together, these changes meant that region of the nonoscillatory state was not observed for some values of D, such that the nonoscillatory state appeared in isolated regions, S_1 and S_2 in Figs. 2(a)(ii) and 2(b)(ii). There was a wide range of inhibitory coupling J_{33} [e.g., 80–120 mV in Fig. 2(b)(ii))], over which the network can switch between nonoscillatory and oscillatory states by varying the lateral delay [white squares in Fig. 2(b)(ii)) and the corresponding spike activity shown in Fig. 4(b), top and middle].

As the strength of synaptic input from E_1 was further increased, two Hopf bifurcation lines defining the O_1 and O_3 states merged and created a small region in the space spanned by J_{33} and D in which the network exhibited nonoscillatory activity S_1 [Figs. 2(a)(iii) and 2(a)(iii)]. Outside of S_1, where O_1 and O_3 merged [e.g., white square in Fig. 2(b)(ii)i)], the slow oscillatory activity induced by the lateral E_1-I_3 loops and the fast oscillatory activity induced by the local I_3-I_3 loop coexisted. This was evident in the power spectrum of inhibitory population firing rate, which showed two peaks at low (25 Hz) and high (100 Hz) frequencies [Fig. 4(d), left bottom]. Moreover, when the population rates were bandpassed filtered at high and slow frequencies and then summed up, the filtered population rates closely followed the actual inhibitory firing rates [Fig. 4(d), top]. Interestingly, in our model amplitude of the fast oscillation was modulated according to the phase of slow oscillation [Fig. 4(d), right bottom]. This

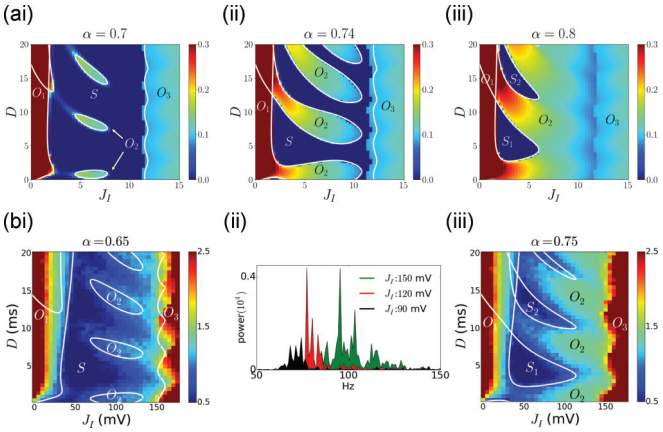

FIG. 5. Composition of three oscillatory states. α denotes the relative strength of E_2-I_3 loop: $J_{23} = \alpha J_I, J_{33} = J_I$. (a) Rate model; $J_{12} = 0.5, J_{13} = 2, J_{32} = 4, J_{21} = J_{31} = 1$, $d = 2.5$, $\tau_d = 0$. (b) Spiking network model; (ii), power spectrum of population I_3's mean firing rates for $D = 7$ ms in (b)(i); total (individual) synaptic weights, $J_{12} = 30(0.03), J_{13} = 60(0.24), J_{32} = 120(0.12), J_{21} = J_{31} = 30(0.06)$ mV, $d = 2.5$ ms, $\tau_d = 1$ ms. Color bars show the coefficient of variations of network models. White lines show analytical estimates of a Hopf bifurcation [Eqs. (A2) and (15)].

was akin to the modulation of γ-band oscillation power by the phase of θ-band oscillation observed in the hippocampus [12,35].

Thus, we showed that when a partially overlapping neuron population participated in the generation of both fast oscillation and slow oscillation (i.e., I_3 is part of the fast I_3-I_3 loop and the slow E_1-I_3 loop), cross-frequency coupling emerged in which slow oscillation generated via the lateral loop (E_1-I_3) with long delay D modulated the amplitude of fast oscillation (I_3-I_3) by providing periodic input.

D. Emergence of an oscillatory state driven by E_2-I_3 coupling

Thus far, we considered oscillatory activity generated by the I_3-I_3 loop. In this section, we describe how including the oscillatory activity due to the E_2-I_3 loop further enriches the dynamical landscape of the three population network. To control the interaction of the E_2-I_3 and I_3-I_3 loops, we introduced a parameter α that determined the relative strength of the E_2-I_3 coupling with respect to I_3-I_3 coupling: $J_{23} = \alpha J_I$, $J_{33} = J_I$.

With weak coupling between E_2-I_3 (i.e., small α), Hopf bifurcation structure was identical to the one obtained by varying J_{33} alone, as shown in Figs. 2(a)(i) and 2(b)(i). In other words, the O_3 state, driven by the I_3-I_3 loop, was the only oscillatory state that can be generated by the E_2I_3 subnetwork. When α was increased, a new oscillatory state O_2, driven by the E_2-I_3 loop, emerged in the small isolated regions in the space spanned by J_1 and D [Figs. 5(a)(i) and 5(b)(i). The O_2 state emerged in a parameter space which led to the nonoscillatory state (S) for low values of α. That is, for high α values, long-range interactions with the population E_1 destabilized the nonoscillatory state of the E_2I_3 subnetwork to create oscillations.

To better understand why nonoscillatory and different oscillatory states appeared as a function of J_I, we fixed the lateral delay [e.g., $D = 9$ in Fig. 5(a)(i)] and examined the changes in network state as J_I increases. For small J_I, local inhibition was too weak to withstand the oscillatory instability driven by the lateral E_1-I_3 loop, so the network entered the O_1 state. The network shifted to the nonoscillatory state S when the local inhibition J_I was increased. When J_I became sufficiently strong to generate oscillatory activity through the E_2-I_3 loop, the network entered O_2 state. When J_I was further increased, the increased I_3-I_3 coupling suppressed the oscillatory activity induced by the E_2-I_3 loop, which brought the network back to the nonoscillatory state. For strong J_I, the I_3-I_3 coupling became the dominant network motif producing oscillatory activity, and hence the network entered the O_3 state.

The O_2 state, however, appeared only within a restricted range of lateral delays [e.g., $7 < D < 10$ in Fig. 5(a)(i)] and vanished gradually outside of this range. As discussed in Sec. IV B, the O_2 state appeared when the oscillatory activity relayed through the lateral connections was in phase with the ongoing oscillations in the E_2I_3 subnetwork. On the other hand, the O_2 state could no longer exist when the relayed network activity no longer enhanced the local activity. Such resonance and cancellation effects, occurring repeatedly, gave rise to isolated O_2 states at multiple sites. The periodic appearance of stationary and oscillatory states is a robust phenomenon in delayed feedback system, which has been investigated in the context of controlling pathological brain rhythms [17,19].

When the E_2-I_3 coupling became stronger (α was increased), the O_2 state expanded across the nonoscillatory state S and merged with the O_1 state, creating a complex configuration of multiple network states as shown in Fig. 5(a)(ii). The O_1 and O_3 states, previously separated by S, were now bridged by an elongated O_2 region. When α was further increased, all three oscillatory states, O_1, O_2, and O_3, appeared contiguously, and the nonoscillatory states formed isolated regions surrounded by the O_1 and O_2 states [Figs. 5(a)(iii) and 5(b)(iii)]. Such a dynamical landscape is similar to the previously discussed bifurcation structure that produced cross-frequency oscillations at a parameter region where multiple Hopf bifurcations meet [see Figs. 2(a)(iii) and 2(b)(iii)].

In networks of spiking neurons, O_2 states emerged from the nonoscillatory state at multiple sites, as predicted by the analysis. However, unlike the dynamical landscape of the firing rate model [Fig. 5(a)(i)], network simulations showed that O_2 states did not exist in isolation. The network activity remained oscillatory in between the O_2 and O_3 states [Fig. 5(b)(i)], and the oscillation frequency increased gradually as the network transitioned from O_2, S, to O_3 [Fig. 5(b)(ii)]. This discrepancy between the analytical prediction and network simulation suggested that the activity of our network model cannot make sharp state transitions as predicted by the Fokker-Planck formulation. This discrepancy is possibly because of the finite-size effects [2]. When α became large as shown in Fig. 5(b)(iii), the O_2 state expanded horizontally across the nonoscillatory state, connected the O_1 and O_3 states, and created isolated nonoscillatory states surrounded by the oscillatory states, O_1 and O_2, similar to the firing rate model [Fig. 5(a)(iii)].

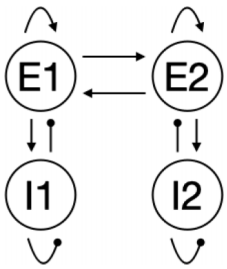

FIG. 6. The connectivity structure of E_1I_1-E_2I_2 network.

E. Essential role of long-range inhibition

We asked if the long-range inhibitory connections were essential for creating network motifs that involved excitatory-inhibitory or inhibitory-inhibitory loops with long delays in the three-population network. To this end, we examined the connectivity motifs of a network of two fully connected E_1I_1 and E_2I_2 networks coupled by long-range excitation between respective excitatory populations (E_1 and E_2) (Fig. 6). In this model, long-range inhibition did not exist in the sense that inhibitory populations were coupled to local excitatory populations but did not interact with the other EI network.

To isolate the crucial network motifs in four population network, we performed the stability analysis to derive an equation analogous to Eq. (10):

$$0 = \begin{vmatrix} -1 + A_{E_1E_1} & -A_{E_1I_1} & A_{E_1E_2} & 0 \\ A_{I_1E_1} & -1 - A_{I_1I_1} & 0 & 0 \\ A_{E_2E_1} & 0 & -1 + A_{E_2E_2} & -A_{E_2I_2} \\ 0 & 0 & A_{I_2E_2} & -1 - A_{I_2I_2} \end{vmatrix}. \tag{21}$$

We defined the coupling matrices for the subnetworks E_1I_2 and E_2I_2 as

$$M_1 = \begin{pmatrix} -1 + A_{E_1E_1} & -A_{E_1I_1} \\ A_{I_1E_1} & -1 - A_{I_1I_1} \end{pmatrix},$$

$$M_2 = \begin{pmatrix} -1 + A_{E_2E_2} & -A_{E_2I_2} \\ A_{I_2E_2} & -1 - A_{I_2I_2} \end{pmatrix}.$$

Then Eq. (21) became

$$0 = |M_1M_2| + A_{E_1E_2}A_{E_2E_1}[A_{I_1E_1}A_{E_2I_2} - (1 + A_{I_1I_1})(1 + A_{I_2I_2})]. \tag{22}$$

where the first term $|M_1M_2|$ was for a network in which the subnetworks E_1I_1 and E_2I_2 were uncoupled, and the second term captured the interaction between two subnetworks through the long-range excitatory connections, $A_{E_1E_2}$ and $A_{E_2E_1}$.

From the stability analysis, we identified five types of motifs that were introduced by the long-range connections between the excitatory populations. The motif $A_{E_1E_2}A_{E_2E_1}A_{I_1E_1}A_{E_2I_2}$ included feedforward excitation ($A_{I_1E_1}$) and feedforward inhibition ($A_{E_2I_2}$) linked to the reciprocal long-range excitatory connections $A_{E_1E_2}A_{E_2E_1}$. The remaining four motifs $A_{E_1E_2}A_{E_2E_1}$, $A_{E_1E_2}A_{E_2E_1}A_{I_1I_1}$, $A_{E_1E_2}A_{E_2E_1}A_{I_2I_2}$, and $A_{E_1E_2}A_{E_2E_1}A_{I_1I_1}A_{I_1I_1}$ involved recurrent excitation between two excitatory populations and recurrent inhibition within inhibitory populations. Note that none of these motifs included the excitatory-inhibitory or inhibitory-inhibitory couplings with long delays which were the source of oscillatory dynamics with multiple frequencies in our study. Thus, this analysis result verified that the long-range inhibitory connections from and to I_3 are essential for creating long-range inhibitory loops present in the three-population model [see Eq. (11)].

V. CONCLUSION

A population of neurons embedded in a larger network rarely acts alone but interacts with neighboring and distant neurons. In the present study, we used a generic network model to investigate how including long synaptic delays may affect the dynamics of a standard model for local cortical circuits. When an additional excitatory population was coupled to a local excitatory-inhibitory network via long-range connections, the lateral delays between them created a rich bifurcation structure, composed of isolated stationary state, multiple oscillatory states, and cross-frequency coupling (Fig. 2). To the best of our knowledge, it is the first time that isolas of nonoscillatory (Fig. 2) and oscillatory (Fig. 5) states have been found in biological neuronal networks consisting of multiple excitatory and inhibitory populations over a wide parameter regime. Our results suggest that long delays observed in the brain can potentially play a significant role in reshaping the local network dynamics.

While the idea of long-range inhibition is inspired from experimental data, we note that we have not modeled any specific brain region. Instead, here our aim has been to characterize to what extent long-range inhibition may affect the dynamics of the standard EI network which models a typical network in the neocortex. The simplicity of the model allowed us to systematically isolate the various motifs that contribute to multifrequency oscillations and emergence of isolas of oscillatory and nonoscillatory activity.

It is interesting to note that cross-frequency oscillations, one of the dynamics found in our model, is also an important feature of population activity recorded from the hippocampus and neocortex of awake behaving animals. The proposed circuit model for the cross-frequency oscillations in hippocampus, however, has a different structure—it consists of one excitatory and two types of inhibitory neurons, where fast spiking and O-LM interneurons are responsible for generating γ (30–80 Hz) and θ (4–12 Hz) rhythms, respectively [12,36]. However, the hippocampus is a target of long-range inhibition from other brain regions, e.g., entorhinal cortex [23]. The long-range inhibition, as predicted by our results, may also contribute to the emergence and control of cross-frequency oscillations in the hippocampus.

The dynamic regime of our network model is defined by the cancellation of excitatory and inhibitory synaptic inputs to individual neurons that result in asynchronous spiking. In this noise-driven regime, the net synaptic current is highly noisy fluctuating around the mean input that remains below the spike threshold [2,4]. The balanced network [1] also operates in the noise-driven regime, but uses $O(1/\sqrt{N})$ scaling of synaptic weights that creates finite noise in the large-N limit. By contrast, our model used $O(1/N)$ scaling of synaptic weights which dilutes the synaptic noise if N becomes infinitely large. Finite, but large, network size allowed our

model to generate noisy synaptic and spiking activity in the network simulations.

We note that the excitatory-excitatory connections in the three-population model did not play a role in generating the oscillatory dynamics investigated in this study. The long excitatory delays between E_1-E_2 populations, however, took part in relaying the oscillatory activity between the E_2I_3 subnetwork and the E_1 population. Moreover, the short recurrent excitatory delays within the E_1 and E_2 populations do not generate oscillatory activities in the standard EI network [2,4], and therefore, we excluded those connections from our model. In a previous work, it was shown that when two local EI networks were coupled via long-range excitatory-excitatory connections, multiple metastable dynamics emerged and switched from one to another spontaneously [37]; however, oscillatory activities with multiple frequencies were not observed in such a network. Our three-population model and analysis on the E_1I_1-E_2I_2 network suggest that the existence of long- and short-range inhibitions may be important for generating oscillatory dynamics with multiple frequencies.

Various effects of time delay on neural dynamics have been studied extensively in neural field equation that models spatial interactions. It has been shown that the delay can induce oscillations for local excitation-lateral inhibition interaction [38], give rise to rich bifurcation structure in a simple scalar model [39], and stabilize stochastic bump attractors [40]. Our results demonstrate that a lumped firing rate model and randomly connected spiking models can also develop rich dynamic repertoire without explicit spatial interactions.

Our network simulations and analysis were restricted to a special case in which all delays were fixed. It would be of interest to study the effects of distributed delays in the future, as in Refs. [41–43], to reflect biologically realistic connectivity and go beyond the three-population motifs.

ACKNOWLEDGMENTS

This work was supported by the BrainLinks-BrainTools Cluster of Excellence funded by the German Research Foundation (DFG EXC 1086), the German Federal Ministry of Education and Research (FKZ 01GQ0830), and the INTERREG IV Rhin superieur program and European Funds for Regional Development through the project TIGER A31 and the Swedish Research Council (2018-03118).

APPENDIX A: CALCULATION OF CRITICAL COUPLINGS

We substitute $\lambda = i\omega$ and calculate the rate response function $R_a(i\omega)$ and the synaptic kernel $\Sigma_{ab}(i\omega)$. For the rate model,

$$R_a^{\mathrm{RM}}(i\omega) = 1/(1+i\tau_a\omega) = C_a\exp(-i\phi_a),$$
$$C_a = \frac{1}{\sqrt{1+\tau_a^2\omega^2}}, \quad \phi_a = \mathrm{atan}(\tau_a\omega),$$

with $0 \leqslant \mathrm{atan}(\tau_a\omega) < \pi/2$, and for the spiking network,

$$R_a^{\mathrm{LIF}}(i\omega) = \tau_{ma}R_a^{\mathrm{THIN}}(i\omega) = C_a\exp(-i\phi_a),$$
$$C_a = \tau_{ma}\left|R_a^{\mathrm{THIN}}\right|, \quad \phi_a = -\arg\left(R_a^{\mathrm{THIN}}\right),$$

where R_a^{THIN} is the population response function obtained numerically from the threshold integration method [29]. The synaptic kernel

$$\begin{aligned}\Sigma_{ab}(i\omega) &= \exp(-i\omega D_{ab})/(1+i\omega\tau_d)\\ &= C_s\exp(-i\phi_s - i\omega D_{ab}),\end{aligned}$$
$$C_s = \frac{1}{\sqrt{1+\omega^2\tau_d^2}}, \quad \phi_s = \mathrm{atan}(\tau_d\omega),$$

with $0 \leqslant \mathrm{atan}(\tau_d\omega) < \pi/2$.

Substituting $R_a(i\omega)$ and $\Sigma_{ab}(i\omega)$ to Eq. 11 yields

$$\begin{aligned}0 = 1 &- c_r\exp(-i\Phi_{12} - i2D\omega) + c_i[\exp(-i\Phi_3 - id\omega)\\ &- c_r\exp(-i\Phi_{123} - i2D\omega - id\omega)]\\ &+ c_{p_0}[c_{p_1}\exp(-i\Phi_{23} - i2d\omega)\\ &+ c_{p_2}\exp(-i\Phi_{123} - i2D\omega - id\omega)]\\ &+ c_t\exp(-i\Phi_{123} - i2D\omega - id\omega)\\ &+ c_d\exp(-i\Phi_{13} - i2D\omega),\end{aligned}$$

where we decompose c_{p_d} and c_{p_i} in Eqs. (12) and (13) in terms of $c_{p_0} = J_{23}A_2A_s$, $c_{p_1} = J_{32}A_3A_s$, and $c_{p_2} = J_{31}J_{12}A_1A_3A_s^2$ in order to explicitly solve for J_{23} in the following calculations.

To study the bifurcation structure when J_{23} are varied, we manipulated Eqs. (12) and (13), as discussed in Sec. III B, to solve for the inhibitory coupling strength $J_{23} = c_{p_0}/(A_2A_s)$:

$$\begin{aligned}Ac_{p_0}^2 + 2Bc_{p_0} + C = 0,\\ c_{p_0} = \frac{1}{A}(-B \pm \sqrt{B^2 - AC}),\end{aligned} \tag{A1}$$

where

$$\begin{aligned}A &= c_{p_2}^2 - c_{p_1}^2,\\ B &= -c_rc_{p_2}\cos(\Phi_3 + d\omega) + (c_dc_{p_2} - c_ic_{p_1})\cos(\Phi_2 + d\omega)\\ &\quad - c_{p_1}\cos(\Phi_{23} + 2d\omega) - c_rc_ic_{p_2} + c_tc_{p_2},\\ C &= c_r^2 + (c_rc_i)^2 + c_d^2 + c_t^2 - c_i^2 - 1\\ &\quad + 2\left[\left(c_r^2c_i - c_i - c_rc_t\right)\cos(\Phi_3 + d\omega)\right.\\ &\quad - c_rc_d\cos(\Phi_3 - \Phi_2)\\ &\quad \left.+ (c_t - c_rc_i)c_d\cos(\Phi_2 + d\omega) - c_rc_ic_t\right].\end{aligned}$$

On the other hand, to study the bifurcation structure when both J_{23} and J_{33} are varied, we similarly manipulate Eqs. (12) and (13) to solve for the inhibitory coupling J_I where $J_{23} = \alpha J_I$ and $J_{33} = J_I$:

$$\begin{aligned}AJ_I^2 + 2BJ_I + C = 0,\\ J_I = \frac{1}{A}(-B \pm \sqrt{B^2 - AC}),\end{aligned} \tag{A2}$$

where

$$\begin{aligned}A &= \left(c_r\bar{c}_i - c_{p_2}\bar{c}_{p_0}\right)^2 - \bar{c}_i^2 - \left(c_{p_1}\bar{c}_{p_0}\right)^2\\ &\quad - 2\bar{c}_ic_{p_1}\bar{c}_{p_0}\cos(\Phi_2 + d\omega),\\ B &= \left(c_r^2\bar{c}_i - c_rc_{p_2}\bar{c}_{p_0} - \bar{c}_i\right)\cos(\Phi_3 + d\omega)\\ &\quad + \left(c_{p_2}\bar{c}_{p_0}c_d - c_r\bar{c}_ic_d\right)\cos(\Phi_2 + d\omega)\\ &\quad - c_{p_1}\bar{c}_{p_0}\cos(\Phi_{23} + 2d\omega) - c_r\bar{c}_ic_t + c_{p_2}\bar{c}_{p_0}c_t,\end{aligned}$$

$$C = c_r^2 + c_d^2 + c_t^2 - 1 + 2[-c_r c_d \cos(\Phi_3 - \Phi_2) - c_r c_t \cos(\Phi_3 + d\omega) + c_d c_t \cos(\Phi_2 + d\omega)],$$

and $\bar{c}_{p_0} = \alpha c_{p_0}/J_{23}$ and $\bar{c}_i = c_i/J_{33}$.

APPENDIX B: PHASE LAG

From the second and third lines of the coefficient matrix, Eq. (10), we can derive

$$\delta r_3 = \frac{A_{31} + A_{32}A_{21}}{1 + A_{33} + A_{23}A_{32}} \delta r_1,$$

which implies that the relative phase difference

$$\Delta\phi_{31} = \arg[(A_{31} + A_{32}A_{21})/(1 + A_{33} + A_{23}A_{32})] \quad \text{(B1)}$$

of I_3 with respect to E_1 is determined by the later couplings, A_{31} and $A_{32}A_{21}$, that connect E_1 to E_3, and the local couplings, A_{33} and $A_{23}A_{32}$. In Fig. 4(b), we numerically evaluate the above $\Delta\phi_{31}$.

On the other hand, for the reduced two-population network considered in Sec. IV B, the first line of Eq. (10),

$$\delta r_3 = -\frac{1}{A_{13}} \delta r_1,$$

gives a simple expression for the phase difference

$$\Delta\phi_{31} = -\pi + \Phi_1 + D\omega.$$

[1] C. van Vreeswijk and H. Sompolinsky, Science **274**, 1724 (1996).
[2] N. Brunel, J. Comput. Neurosci. **8**, 183 (2000).
[3] N. Brunel and X.-J. Wang, J. Neurophysiol. **90**, 415 (2003).
[4] E. Ledoux and N. Brunel, Front. Comput. Neurosci. **5**, 25 (2011).
[5] S. Ostojic, Nat. Neurosci. **17**, 594 (2014).
[6] S. Denève and C. K. Machens, Nat. Neurosci. **19**, 375 (2016).
[7] S. Sadeh, S. Cardanobile, and S. Rotter, SpringerPlus **3**, 148 (2014).
[8] B. K. Murphy and K. D. Miller, Neuron **61**, 635 (2009).
[9] A. Kumar, S. Schrader, A. Aertsen, and S. Rotter, Neural Comput. **20**, 1 (2008).
[10] P. Fries, Annu. Rev. Neurosci. **32**, 209 (2009).
[11] G. Hahn, A. F. Bujan, Y. Frégnac, A. Aertsen, and A. Kumar, PLoS Comput. Biol. **10**, e1003811 (2014).
[12] A. Hyafil, A. L. Giraud, L. Fontolan, and B. Gutkin, Trends Neurosci. **38**, 725 (2015).
[13] A. Palmigiano, T. Geisel, F. Wolf, and D. Battaglia, Nat. Neurosci. **20**, 1014 (2017).
[14] A. Roxin, N. Brunel, and D. Hansel, Phys. Rev. Lett. **94**, 238103 (2005).
[15] A. Roxin and E. Montbrió, Phys. D (Amsterdam, Neth.) **240**, 323 (2011).
[16] J. Kremkow, A. Aertsen, and A. Kumar, J. Neurosci. **30**, 15760 (2010).
[17] M. Rosenblum and A. Pikovsky, Phys. Rev. E **70**, 1 (2004).
[18] O. V. Popovych, C. Hauptmann, and P. A. Tass, Phys. Rev. Lett. **94**, 164102 (2005).
[19] I. Vlachos, T. Deniz, A. Aertsen, and A. Kumar, PLoS Comput. Biol. **12**, e1004720 (2016).
[20] Z. V. Guo, H. K. Inagaki, K. Daie, S. Druckmann, C. R. Gerfen, and K. Svoboda, Nature (London) **545**, 181 (2017).
[21] K. A. Phillips, C. D. Stimpson, J. B. Smaers, M. A. Raghanti, B. Jacobs, A. Popratiloff, P. R. Hof, and C. C. Sherwood, Proc. R. Soc. London, Ser. B **282**, 20151535 (2015).
[22] R. Caminiti, F. Carducci, C. Piervincenzi, A. Battaglia-Mayer, G. Confalone, F. Visco-Comandini, P. Pantano, and G. M. Innocenti, J. Neurosci. **33**, 14501 (2013).
[23] S. Melzer, M. Michael, A. Caputi, M. Eliava, E. C. Fuchs, M. A. Whittington, and H. Monyer, Science **335**, 1506 (2012).
[24] N. Yamawaki, X. Li, L. Lambot, L. Y. Ren, J. Radulovic, and G. M. Shepherd, Nat. Neurosci. **22**, 618 (2019).
[25] A. Saunders, I. A. Oldenburg, V. K. Berezovskii, C. A. Johnson, N. D. Kingery, H. L. Elliott, T. Xie, C. R. Gerfen, and B. L. Sabatini, Nature (London) **521**, 85 (2015).
[26] S. Krabbe, J. Gründemann, and A. Lüthi, Biol. Psychiatry **83**, 800 (2018).
[27] A. Bertero, P. L. C. Feyen, H. Zurita, and A. junior Apicella, J. Neurosci. **39**, 8424 (2019).
[28] C. T. McDonald and A. Burkhalter, J. Neurosci. **13**, 768 (1993).
[29] M. J. E. Richardson, Phys. Rev. E **76**, 021919 (2007).
[30] M.-O. Gewaltig and M. Diesmann, Scholarpedia **2**, 1430 (2007).
[31] C. Börgers and N. Kopell, Neural Comput. **15**, 509 (2003).
[32] P. H. Tiesinga, J.-M. Fellous, J. V. José, and T. J. Sejnowski, Hippocampus **11**, 251 (2001).
[33] X.-J. Wang and G. Buzsáki, J. Neurosci. **16**, 6402 (1996).
[34] A. Viriyopase, R.-M. Memmesheimer, and S. Gielen, J. Neurophysiol. **116**, 232 (2016).
[35] L. L. Colgin, T. Denninger, M. Fyhn, T. Hafting, T. Bonnevie, O. Jensen, M.-B. Moser, and E. I. Moser, Nature (London) **462**, 353 (2009).
[36] A. B. L. Tort, H. G. Rotstein, T. Dugladze, T. Gloveli, and N. J. Kopell, Proc. Nat. Acad. Sci. USA **104**, 13490 (2007).
[37] K. M. Kutchko and F. Fröhlich, PLoS Comput. Biol. **9**, e1003304 (2013).
[38] A. Hutt, Phys. Lett. A **372**, 541 (2008).
[39] R. Veltz, SIAM J. Appl. Dyn. Syst. **12**, 1566 (2013).
[40] Z. P. Kilpatrick, Phys. D (Amsterdam, Neth.) **295**, 30 (2015).
[41] C. G. Assisi, V. K. Jirsa, and J. A. Scott Kelso, Phys. Rev. Lett. **94**, 018106 (2005).
[42] F. M. Atay and A. Hutt, SIAM J. Appl. Dyn. Syst. **5**, 670 (2006).
[43] S. Petkoski, A. Spiegler, T. Proix, P. Aram, J.-J. Temprado, and V. K. Jirsa, Phys. Rev. E **94**, 012209 (2016).